Structural transition in the magnetoelectric ZnCr_{2}Se_{4} spinel under pressure

I. Efthimiopoulos, Z. T. Y. Liu, S. V. Khare, P. Sarin, V. Tsurkan, A. Loidl, D. Popov, and Y. Wang

Phys. Rev. B **93**, 174103 — Published 9 May 2016

DOI: 10.1103/PhysRevB.93.174103

Structural transition in the magnetoelectric $ZnCr_2Se_4$ spinel under pressure

I. Efthimiopoulos[1,*,†], Z. T. Y. Liu[2,*], S. V. Khare[2], P. Sarin[3], V. Tsurkan[4,5], A. Loidl[4], D. Popov[6], and Y. Wang[1,‡]

[1]*Department of Physics, Oakland University, Rochester, Michigan 48309, USA*

[2]*Department of Physics, University of Toledo, Toledo, Ohio 43606, USA*

[3]*School of Materials Science and Engineering, Oklahoma State University, Tulsa, Oklahoma 74106, USA*

[4]*Institute of Applied Physics, Academy of Sciences of Moldova, MD-2028 Chisinau, Republic of Moldova*

[5]*Experimental Physics 5, Center for Electronic Correlations and Magnetism, Institute of Physics, University of Augsburg, D-86159 Augsburg, Germany*

[6]*High Pressure Collaborative Access Team, Geophysical Laboratory, Carnegie Institution of Washington, Argonne, Illinois 60439, USA*

The magnetoelectric $ZnCr_2Se_4$ spinel, with space group $Fd\bar{3}m$, undergoes a reversible first-order structural transition initiating at 17 GPa, as revealed by our high-pressure X-ray diffraction studies at room temperature. We tentatively assign the high-pressure modification to a AMo_2S_4-type phase, a distorted variant of the monoclinic Cr_3S_4 structure. Furthermore, our Raman investigation provides evidence for a pressure-induced insulator-metal transition. Our density functional theory calculations successfully reproduce the structural transition. They indicate significant band gap and magnetic moment reduction accompanying the pressure-induced structural modification. We discuss our findings in conjunction with the available high-pressure results on other Cr-based chalcogenide spinels.

PACS number(s): 61.50.Ks, 71.20.-b, 75.50.Pp

I. INTRODUCTION

Ternary Cr-bearing compounds of the $A^{2+}Cr^{3+}{}_2X^{2-}{}_4$ (A^{2+} = Ti-Zn, Cd, Hg; X^{2-} = O, S, Se) stoichiometry are commonly found in two different structural polymorphs at ambient conditions[1–3]. One of these structural classes is the cubic spinel phase (SG $Fd\bar{3}m$, Z = 8, **Fig. 1**), which is composed of AX_4 tetrahedral and edge-sharing CrX_6 octahedral units. The spinel structure presents a prototype system for studying magnetic interactions in solids, mainly due to the geometric frustration of the magnetic Cr^{3+} cations residing in a pyrochlore lattice[4,5]. The other structural group for the $A^{2+}Cr^{3+}{}_2X^{2-}{}_4$ compounds is the monoclinic Cr_3S_4-type phase (SG $C2/m$, Z = 2), which can be viewed as a defect variant of the hexagonal NiAs-type structure with ordered vacancies[6]. Both types of cations are octahedrally coordinated with respect to the anions in this phase, i.e. the Cr_3S_4-type structure has a higher density than the spinel phase. Therefore, this monoclinic Cr_3S_4-type phase can be viewed as a high-pressure structural candidate for the spinel members of this series.

All of the oxide members of the $A^{2+}Cr^{3+}{}_2O^{2-}{}_4$ series adopt the spinel structure at ambient conditions. Upon comression and/or heating, the oxide spinels tend to adopt a denser orthorhombic $CaTi_2O_4$-, $CaMn_2O_4$-, or $CaFe_2O_4$-type phase[7–11], occasionally through an intermediate tetragonal structure (SG $I4_1/amd$, Z = 4)[12–14]. A transformation from the cubic phase towards the Cr_3S_4-type structure has not been reported for any oxide Cr-spinel.

On the other hand, the $A^{2+}Cr^{3+}{}_2(S, Se)^{2-}{}_4$ chalcogenides crystallize in either the spinel structure or the Cr_3S_4-type phase at ambient conditions, depending on the type of the A cation[2]. In particular, Cr-based sulphides with A^{2+} = Mn, Fe, Co, Cu, Zn, Cd, and Hg adopt the spinel structure, whereas materials with A^{2+} = Ti, V, Cr, and Ni crystallize in the Cr_3S_4-type phase. High-pressure and/or high temperature is known to to tranform the Mn, Fe, and Co thiospinels into the denser Cr_3S_4-type phase[15]. These structural transitions are accompanied by significant alterations in the magnetic and electronic properties[2,16]. Finally, the vast majority of selenides favor the the Cr_3S_4-type phase (A^{2+} = Ti, V, Cr, Ni, Mn, Fe, and Co); materials with A^{2+} = Cu, Zn, Cd, and Hg adopt the spinel structure[6]. The only recorded example of a selenide spinel transforming into a Cr_3S_4-type phase is $CdCr_2Se_4$, which was reported to adopt a monoclinic superstructure of Cr_3S_4 at combined pressure and high-temperature conditions[1].

Previous studies at ambient pressure show that $ZnCr_2Se_4$ undergoes a coupled magneto-structural transition below ~20 K[17–22], whereas another structural transformation of the cubic structure into an unknown phase occurs at high temperatures[23]. Given this structural instability with varying temperature along with the strong spin-lattice coupling active in this system, the application of external pressure presents an appealing variable for further exploring and tuning the physical properties of this compound. Indeed, a recent high-pressure optical investigation

detected electronic changes initiating beyond 11 GPa[24]; the authors attributed this behavior to a pressure-induced structural modification.

Partly motivated by the aforementioned study, we have investigated the structural and vibrational properties of $ZnCr_2Se_4$ under pressure. Our high-pressure X-ray diffraction (XRD) study at room temperature shows that $ZnCr_2Se_4$ undergoes a reversible structural transformation from the starting spinel phase towards a monoclinic structure initiating at 17 GPa. Our high-pressure Raman investigation evidences the substantial reduction of Raman intensity above 12.5 GPa, in agreement with the aforementioned IR study[24]. Finally, our *ab initio* density functional theory (DFT) studies successfully reproduce the cubic-monoclinic structural transition; in addition, the calculations indicate significant magnetic moment and band gap reduction accompanying the structural modification.

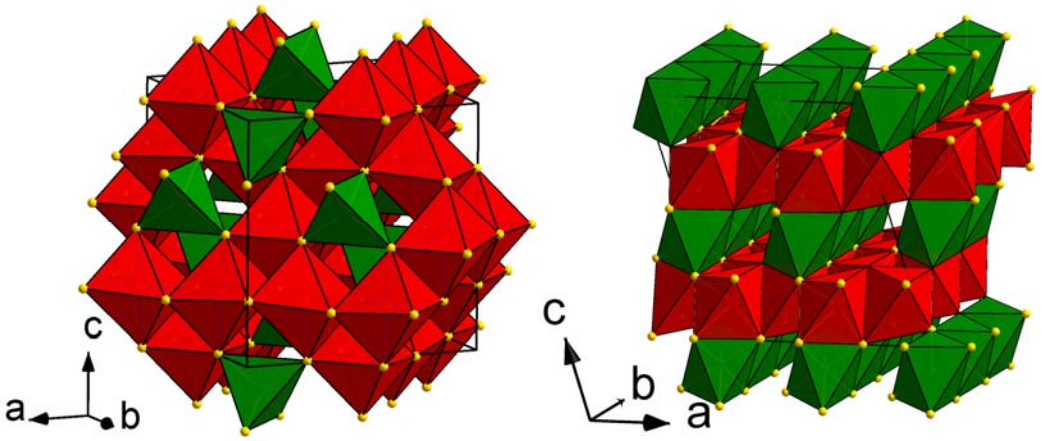

FIG. 1: (Color online) Polyhedral representation of the ambient-pressure spinel structure (SG $Fd\bar{3}m$, $Z = 8$, left) and the *potential* high-pressure monoclinic phase of $ZnCr_2Se_4$ (SG Cc, $Z = 8$, right, see text). The green polyhedra correspond to $ZnSe_4$ (left) and $ZnSe_6$ (right) units, whereas the red polyhedra represent the $CrSe_6$ cages. The Se ions are displayed as yellow spheres.

II. EXPERIMENTAL AND COMPUTATIONAL DETAILS

Details of the sample synthesis have been reported elsewhere[21]. Pressure was generated with a gasketed diamond anvil cell (DAC), equipped with a set of diamonds with 300 μm culet diameter. The ruby luminescence method[25] was employed for measuring pressure.

The angle-resolved high-pressure powder XRD measurements were performed at the 16BM-D beamline of the High Pressure Collaborative Access Team, at the Advanved Photon Source of Argonne National Laboratory. The incident monochromatic X-ray beam energy was $E = 29.2$ keV ($\lambda = 0.4246$ Å), whereas the sample-detector distance was 318 mm. The measured XRD diffractograms were processed with the FIT2D software[26]. Refinements were performed using the GSAS+EXPGUI software packages[27,28]. The *P-V* data were fitted with Birch-

Murnaghan equation of state (B-M EOS)[29] for both phases. Helium served as a pressure transmitting medium (PTM).

High-pressure Raman experiments were conducted on single-crystalline $ZnCr_2Se_4$ samples with a solid-state laser (λ = 532 nm), coupled to a single-stage Raman spectrometer. Both helium and a mixture of methanol-ethanol-water 16:3:1 served as PTM in separate runs, yielding identical results.

The *ab initio* DFT calculations were performed with the Vienna Abinitio Simulation Package (VASP)[30–33] using the projector-augmented wave method (PAW)[34,35] with Purdew–Burke–Ernzerhoff (PBE) generalized gradient approximation (GGA)[36,37]. Potentials of Zn, Cr_pv, and Se were chosen, where "_pv" denotes that the semi-core 3p electrons of Cr were also included. The plane wave cutoff energy was chosen to be 360 eV to ensure lattice parameter relaxations. During the electronic iterations, Gaussian smearing was used with a sigma value as small as 0.02 eV, until the convergence criterion of 10^{-5} eV was reached.

Since the spinel-monoclinic structural transition was experimentally recorded at room temperature, and temperature is known to put the magnetic moments in disorder, we constructed both cubic and monoclinic structures with paramagnetic configuration for Cr^{3+} using the special quasi-random structure (SQS) generation algorithm[38,39] provided as the program mcsqs in the Alloy Theoretic Automated Toolkit (ATAT)[40,41] for direct comparison with the experiment. Detailed information is provided in the Supplemental Material[42].

To observe the pressure dependence and obtain the equilibrium lattice parameters, we picked 5 or more volume values covering the equilibrium volume and fitted the total energy values to a B-M EOS[29]. During each run, the cell shape, volume, and atomic positions were allowed to freely relax until forces were below 0.01 eV/Å, similar to earlier works[43–48]. If this value could not be reached afer more than 100 steps, an energy criterion of 1 meV per atom was used. We then obtained the pressure values of each volume from the $P(V)$ formulation of the same EOS. Since the SQS supercells were not chosen in the shape of the conventional unit cells for both structures, and symmetry is broken for these SQS cells, symmetrization and idealization was carried out as a post-processing step using the pymatgen interface[49] for the spglib. The symmetry finding tolerance of the class pymatgen.symmetry.analyzer.SpacegroupAnalyzer was set to be 0.3, a rather liberal value.

Finally, the site-projected and orbital-resolved density of states (DOS) were calculated using the tetrahedron method with Blöch corrections[50] and k-points meshes with a KPPRA of 2000. The energy axis from -10 to 5 eV relative to the Fermi energy was sampled with 4000 points.

III. RESULTS AND DISCUSSION

A. Vibrational and structural response of $ZnCr_2Se_4$ under pressure

As a first step for resolving the high-pressure structural behavior of $ZnCr_2Se_4$, we have performed Raman spectroscopic investigations (**Fig. 2**). We could detect four (out of the five expected) Raman-active modes for the spinel phase[51]. The $Fd\bar{3}m$ Raman features phase could be followed up to ~12.5 GPa. Beyond that pressure, the Raman spectra become rather featureless, hinting a transition of $ZnCr_2Se_4$ [**Fig. 2(a)**]. Such pressure-induced behavior can be attributed either to structural disorder[52] and/or electronic effects coming into play under pressure, e.g. an insulator-metal transition[53]. Given that we have no evidence of structural disorder from our XRD study (**Fig 3**), we tend to interpret the vanishing of the Raman signal of $ZnCr_2Se_4$ as a pressure-induced insulator-metal transition. Indeed, our assignment is supported by the recent optical study of Rabia *et al.*, where an increase of infrared (IR) reflectance was observed in-between 11-14 GPa[24]. The extended pressure range of the $ZnCr_2Se_4$ transition between the Raman and IR investigations can be accounted for by the quasi-hydostatic sample environment of the latter study (CsI powder as PTM)[24]. The pressure-induced transition observed in our Raman study is reversible upon decompression (**Fig. 2**).

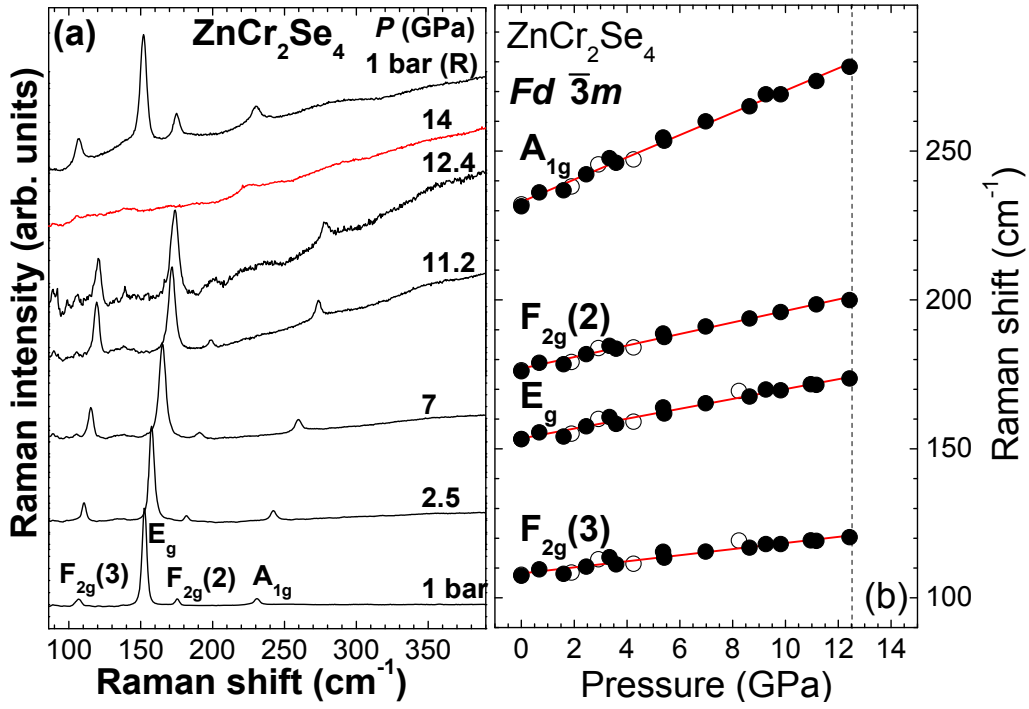

FIG. 2: (Color online) (a) Selected Raman spectra of $ZnCr_2Se_4$ at various pressures (λ = 532 nm, T = 300 K). (b) Raman mode frequency evolution against pressure. Closed and open circles depict measurements upon compression and decompression, respectively. The vertical dashed line represents the onset of the transition.

Selected XRD patterns of $ZnCr_2Se_4$ are presented in **Fig. 3(a)**. The starting $Fd\bar{3}m$ phase persists up to ~15 GPa. Upon further pressure increase, the appearance of several new Bragg peaks indicate a structural transition [**Fig. 3(a)**]. These new features dominate the XRD spectra at 18 GPa, marking the complete structural transformation of the spinel phase. The onset pressure for the transition follows the empirical trend established for AB_2X_4 compounds in terms of their cationic radii[54]. The $Fd\bar{3}m$ spinel phase is recovered upon decompression, consistent with our Raman investigation. We note that there exists a ~4 GPa deviation in the transition pressures observed in our Raman and XRD studies, implying that the proposed insulator-metal transition *precedes* the structural transformation. We discuss this discrepancy in **Section III. D**.

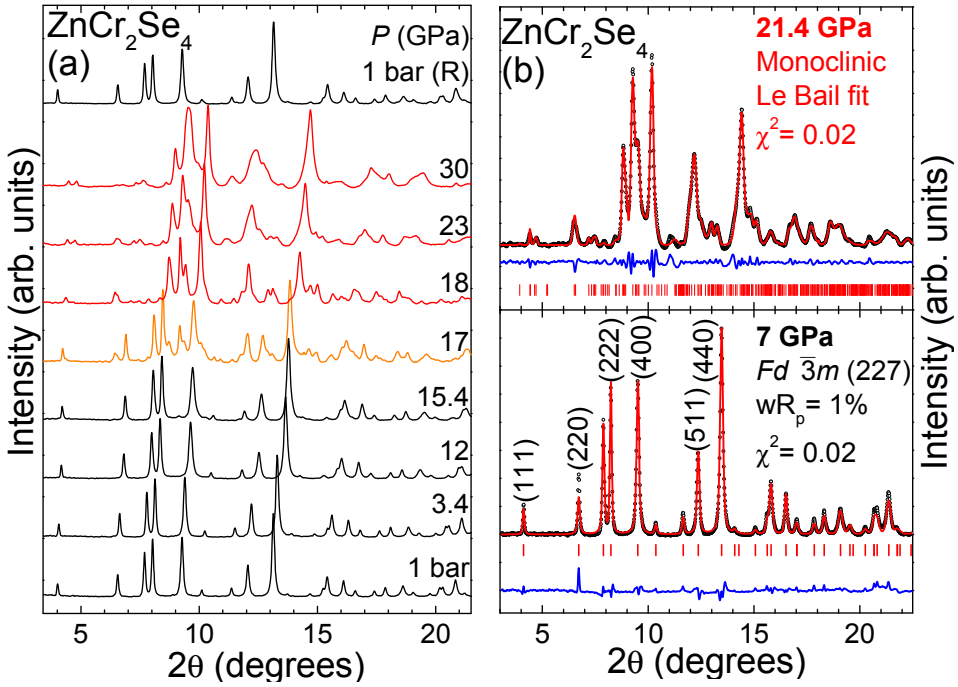

FIG. 3: (Color online) (a) XRD patterns of $ZnCr_2Se_4$ at selected pressures (T = 300 K, λ = 0.4246 Å). The various phases are indicated by different colors: black for $Fd\bar{3}m$, red for the monoclinic, and orange for the coexistence regime. Background has been subtracted for clarity. (b) Refinements of $ZnCr_2Se_4$ XRD patterns at 7 GPa (Rietveld, bottom) and at 21.4 GPa (Le Bail, top). Dots stand for the measured spectra, the red solid lines represent the best refinements, and their difference is drawn as blue lines. Vertical ticks mark the Bragg peak positions.

B. The high-pressure phase of $ZnCr_2Se_4$

By taking into account the available literature[55–57], we attempted to refine the XRD patterns of the $ZnCr_2Se_4$ high-pressure phase with a tetragonal structure ($I4_1/amd$, $Z = 4$), a Ag_3O_4-type phase (SG $P2_1/c$, $Z = 2$), a Li_2CrCl_4-type structure (SG $C2/m$, $Z = 2$), and a Cr_3S_4-type modification (SG $C2/m$, $Z = 2$). None of these structures, however, could reproduce the observed XRD patterns.

On the other hand, the new high-pressure could be indexed with a *monoclinic* unit cell with dimensions approximately a =11 Å, b = 6.8 Å, c = 13 Å, β = 113°, and V = 895 Å^3 at 21.4 GPa, thus hinting Z = 8 for the new structural modification. Unfortunately, both the significant overlap of Bragg reflections [**Fig. 3(b)**] and the development of high texture effects after the structural transformation hindered the determination of a space group and consequent Rietveld refinements. Nevertheless, our estimated unit cell parameters approximated the respective room-temperature values of the $A^{2+}Mo_2S_4$ (A^{2+} = V, Cr, Fe, Co) series [SG *Cc*, Z = 8, **Fig. 1**][58], a distorted variant of the Cr_3S_4-type phase[59]. In this structure, both types of cations exhibit sixfold coordination with respect to the anions, with alternating layers containing either AS_6 or MoS_6 stacked along *c*-axis (**Fig. 1**). Thus, by taking into account **(a)** the coincidence of the unit cell parameters between our high-pressure $ZnCr_2Se_4$ phase and the $A^{2+}Mo_2S_4$ series, **(b)** the structural similarity of the latter with the Cr_3S_4-type phase adopted by several ACr_2Se_4 compounds[6], and **(c)** the transition of the $CdCr_2Se_4$ spinel towards a Cr_3S_4-type superstructure under combined high-pressure and high-temperature conditions[1], we propose that the high-pressure modification of $ZnCr_2Se_4$ can be described with a AMo_2S_4-type structure.

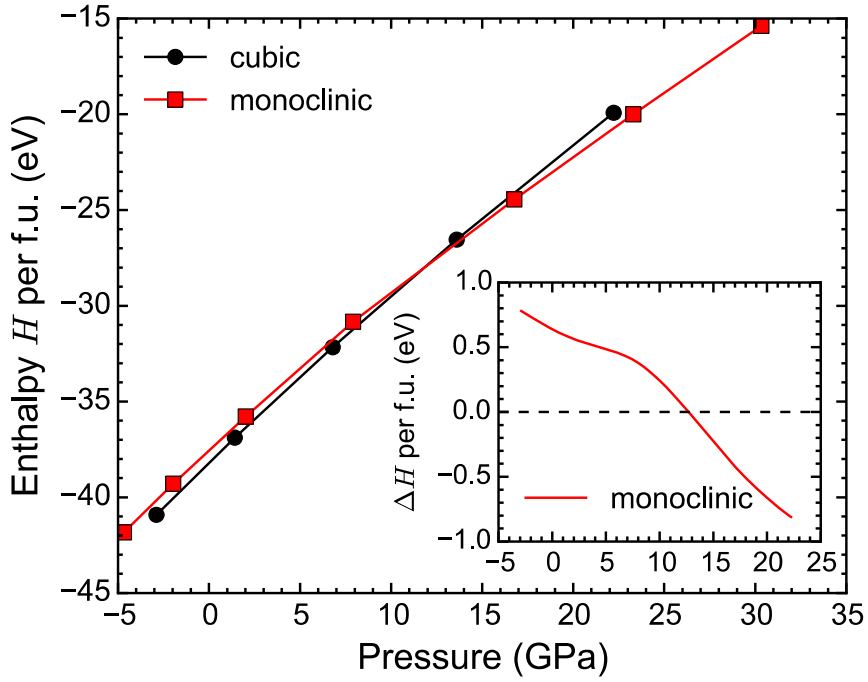

FIG. 4: (Color online) Enthalpy $H = E + PV$ per formula unit (f. u.) of the paramagnetic cubic (black circles) and the paramagnetic monoclinic (red squares) phases of $ZnCr_2Se_4$ as a function of pressure. The inset shows the difference $\Delta H = H$(monoclinic) – H(cubic) between the interpolated values of each phase. ΔH falls below 0 at 12.7 GPa.

In order to verify the experimental cubic-monoclinic transition, we have determined the structural stability for the $Fd\bar{3}m$ and the proposed AMo_2S_4-type structures of $ZnCr_2Se_4$ under pressure via *ab initio* DFT calculations. In **Fig. 4** we

show the calculated enthalpy values $H = E + PV$ for the paramagnetic cubic and monoclinic phases of $ZnCr_2Se_4$ at various pressures. It is clear that the structural transition is reproduced near 13 GPa. Even though the calculated transition pressure P_{Tr} resides slightly lower than its XRD counterpart ($P_{Tr} \approx 17$ GPa), such discrepancy can be accounted for by the negligence of temperature effects in our calculations.

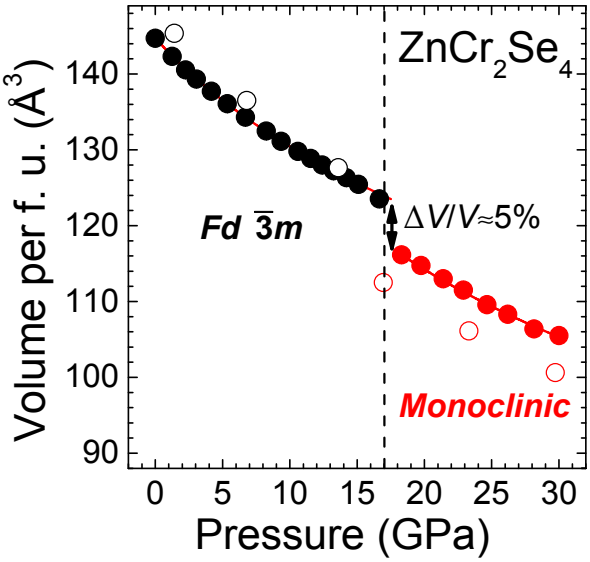

FIG. 5: (Color online) Unit cell volume per formula unit (f. u.) as a function of pressure for both phases of $ZnCr_2Se_4$ (error bars lie within the symbols). The dashed line marks the structural transition pressure. The open symbols correspond to structural data from DFT calculations.

In **Fig. 5** we present the experimental and calculated *P*-*V* data of the $Fd\bar{3}m$ and the monoclinic high-pressure phases of $ZnCr_2Se_4$. The respective lattice parameters and the $Fd\bar{3}m$ interatomic parameters are provided in the Supplementary Material[42]. As we can observe, the cubic-monoclinic transition exhibits a sizeable volume decrease at the transition point (~5%), due to the coordination increase of Zn^{2+} with respect to Se^{2-} from fourfold to sixfold (**Fig. 1**). We note that the calculated cubic structural parameters are very close to the experimentally determined values; on the other hand, the respective values for the monoclinic phase exhibit deviations of ~3-4% (**Fig. 5**)[42]. Such structural discrepancies are well-known effects within DFT calculations with GGA-PBE functionals. Fitting of the experimental and calculated *P*-*V* data with B-M EOS[29] functions for both phases yields the respective elastic parameters (**Table I**). Our $Fd\bar{3}m$ bulk modulus B_0 value is smaller than a previous high-pressure study[60], with the discrepancy arising probably from the different experimental conditions, i.e. the PTM employed in each investigation.

TABLE I: Elastic parameters for both phases of $ZnCr_2Se_4$, resulted from the experimental and calculated *P*-*V* data fitting. Each parameter is evaluated at a reference pressure P_R. Relevant data for other selenide Cr-spinels are also displayed for comparison.

Compound	Phase	PTM	P_R (GPa)	V_{Tr}/Z (Å^3)	B_{Tr} (GPa)	B'_{Tr}
$ZnCr_2Se_4$	***Fd$\bar{3}$m*** (exp.)	Helium	10^{-4}	144.7	74.2(8)	4.9(2)
$ZnCr_2Se_4$	***Fd$\bar{3}$m*** (DFT)	N/A	10^{-4}	148.1	74.1	2.9
$ZnCr_2Se_4$	***Fd$\bar{3}$m*** (exp.)[60]	M/E/W	10^{-4}	142.4	98(2)	N/A
$ZnCr_2Se_4$	***Fd$\bar{3}$m*** (DFT)[61]	N/A	10^{-4}	137.9	78.4(7)	3.96(6)
$CuCr_2Se_4$	***Fd$\bar{3}$m*** (exp.)[60]	M/E/W	10^{-4}	138.9	96(3)	N/A
$CdCr_2Se_4$	***Fd$\bar{3}$m*** (exp.)[62]	M/E/W	10^{-4}	155	101.2(2)	5.2(1)
$HgCr_2Se_4$	***Fd$\bar{3}$m*** (exp.)[57]	Helium	10^{-4}	155.2	77.7(7)	4(fixed)
$ZnCr_2Se_4$	***Monoclinic*** (exp.)	Helium	18.3	116.2	98(1)	4(fixed)
$ZnCr_2Se_4$	***Monoclinic*** (DFT)	N/A	18.3	110.8	113.9	3.6

C. Effect of pressure on the electronic and magnetic properties

Having established the cubic-monoclinic structural transition both from our experiment and calculations, we now focus on possible pressure-induced electronic and/or magnetic effects accompanying this structural modification. In **Fig. 6** we show the calculated electronic density of states (DOS) for both the cubic and monoclinic phases of $ZnCr_2Se_4$ at two different pressures assuming a paramagnetic configuration. For the cubic phase, the top of the valence band (VBM) is composed of Cr-t_{2g} orbital states with a strong admixture of Se-*p* states, whereas the bottom of the conduction band (CBM) is formed primarily by Cr-e_g states. Even though the ideal picture of an octahedrally coordinated Cr^{3+} has no electrons in the Cr-e_g states, we still find some states between -4 eV and -2 eV. One plausible explanation is that the Se^{2-} ligands are not ideal, leading to partial charge transfer (ideally 3*e*). Another explanation might be that the orbital splitting technique employed by the DFT package assigns part of the Cr-Se bonding electrons to the Cr-e_g orbital. Furthermore, the cubic phase is accurately described as insulating at ambient pressure (E_g^{calc} = 0.75 eV), consistent with the experimental picture at room temperature (E_g^{exp} = 1.285 eV)[63]. The numerical band gap E_g discrepancy comes from the well-known E_g underestimation of the DFT approach. Upon compression, more Cr-t_{2g} states participate in the CBM, followed by a concomitant band gap decrease (E_g^{calc} = 0.49 eV at 20 GPa).

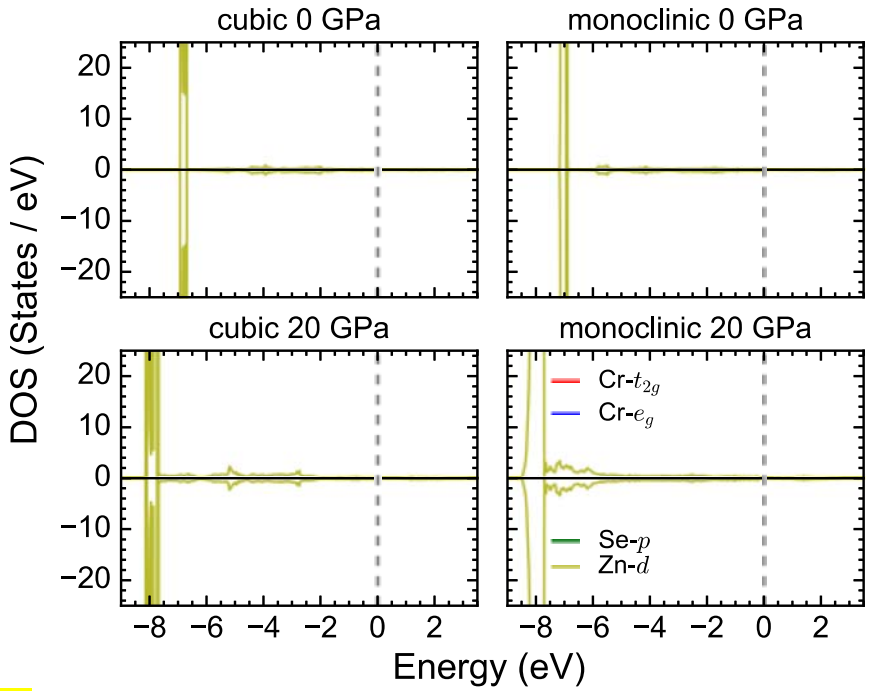

FIG. 6: (Color online) Element-projected and orbital-resolved density of states (DOS) of the paramagnetic cubic and monoclinic phases of $ZnCr_2Se_4$ at two different pressures, 0 and 20 GPa. The spin-up and spin-down states lie above and below the y-axis, respectively. The red lines represent the Cr-t_{2g} orbitals, blue for Cr-e_g orbitals, green for Se-p orbitals, and yellow for the Zn-d states.

For the monoclinic phase, the VBM is primarily formed by Cr-t_{2g}, Se-p, and more Cr-e_g states than the cubic phase, whereas the CBM is mostly composed of Cr-t_{2g} bands. Increasing pressure leads to the particpation of more Cr-e_g states in the CBM. This orbital contribution difference in the DOS between the cubic and monoclinic phases is caused by the distortion of the Se^{2-} octahedra surrounding the Cr^{3+} cations, which is more prominent in the monoclinic structure and "pushes" more electrons to the e_g orbitals. Regarding the band gap value, the monoclinic structure shows a E_g^{calc} of 0.36 eV at ambient pressure, which drops to 0.06 eV at 20 GPa. In other words, $ZnCr_2Se_4$ has undergone a substantial band gap reduction upon adopting the monoclinic structure. We note finally that due to the full shell structure of Zn-d electrons, the latter remain isolated for both phases (**Fig. 6**); the remaining orbitals not shown in the DOS, do not have any significant contributions either.

In order to examine the cubic-monoclinic transition in a more elaborate manner, we have calculated the pressure-induced response of the bulk band gap E_g and the average magnetic moment μ of Cr^{3+}. As we can observe, compression of both phases leads to the gradual decrease for both of these physical quantities. Upon passing into the structural stability regime of the monoclinic phase, i.e. beyond 13 GPa, we can observe significant changes of E_g and μ of Cr^{3+} (**Fig. 7**, from black to red line along the vertical dashed line). Besides the bulk band gap reduction mentioned before (**Fig.**

6), the magnetic moment μ of Cr^{3+} becomes almost halved, from 2.7 μ_B to 1.5 μ_B. Upon pressurizing the monoclinic phase beyond 13 GPa, μ of Cr^{3+} keeps decreasing. Extrapolation of the monoclinic μ of Cr^{3+} indicates that a zero magnetic moment, i.e. a non-magnetic solution will be reached beyond 70 GPa. Similar trends towards non-magnetic configurations have been observed also for the high-pressure phases of $FeCr_2S_4$[55], $HgCr_2S_4$[64], and $HgCr_2Se_4$[57].

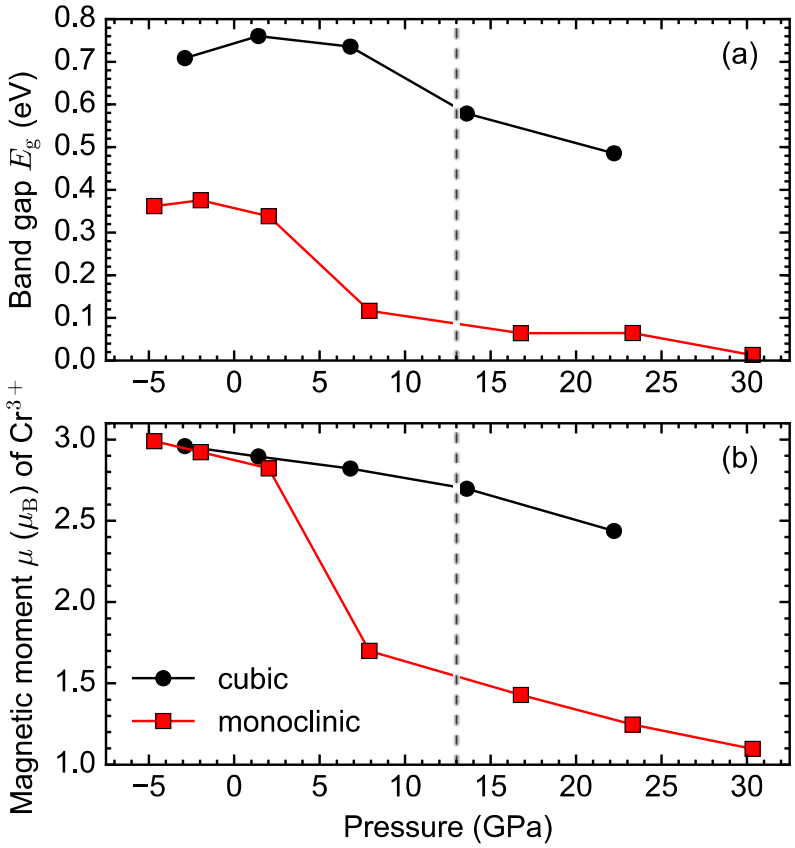

FIG. 7: (Color online) (a) Band gap and (b) average magnetic moment of Cr^{3+} in the paramagnetic cubic and monoclinic phases of $ZnCr_2Se_4$ as a function of pressure.

D. Comparison with other Cr- chalcogenide spinels

Compression of the chromium spinel sulphides at ambient temperature reveals somewhat diverse results. In particular, $FeCr_2S_4$ adopts the Cr_3S_4-type structure at 15 GPa[55]; the mixed $Cu_{0.5}Fe_{0.5}Cr_2S_4$ spinel exhibits also the same high-pressure behavior[65]. $CoCr_2S_4$ undergoes a structural transition towards an undientified phase at 8.5 GPa[66], whereas $HgCr_2S_4$ undergoes three structural transitions up to 40 GPa ($Fd3\square m \rightarrow I4_1/amd \rightarrow$Orthorhombic$\rightarrow$HP3)[64]. Finally, $ZnCr_2S_4$ exhibits signs of amorphization beyond 10 GPa[67]; a more recent study, however, indicates a high-pressure structural behavior similar to $HgCr_2S_4$[68]. On the other hand, combined high-pressure and high-temperature treatment transforms the $MnCr_2S_4$, $FeCr_2S_4$, and

$CoCr_2S_4$ spinels into Cr_3S_4-type phases[15]. Analogous studies on the selenide Cr-spinels reveal that both $CdCr_2Se_4$[69] and $HgCr_2Se_4$[57] undergo tetragonal distortions at 10 GPa and 15 GPa at room temperature, respectively, with $HgCr_2Se_4$ exhibiting signs of disorder upon further compression. Furthermore, $CdCr_2Se_4$ was reported to adopt a Cr_3S_4-type superstructure at combined pressure and high-temperature conditions[1].

Despite the aforementioned investigations, a criterion for the stability range between the spinel and Cr_3S_4-type phases has yet to be established. From an empirical point of view, it is clear that the monoclinic structure is favored for A^{2+} cations with non-filled outer *d* shells; in addition, this phase is more common for selenides than sulphides[2]. The latter implies that the electronegativity of the anion ($Se^{2-} > S^{2-}$) should also influence the structural stability. Taking these considerations into account, $ZnCr_2Se_4$ represents the *first* example of a spinel with closed-shell A^{2+} cations adopting such a monoclinic (super)structure under sufficient compression at *ambient temperature*. Our observation may thus serve as a starting point for unraveling the structural systematics of these interesting systems.

Regarding the possible driving force behind the cubic-monoclinic structural modification, similar transitions observed in $FeCr_2S_4$[55] and $Cu_{0.5}Fe_{0.5}Cr_2S_4$[65] were attributed to a pressure-induced Mott transition of the Fe^{2+} cations and a combination of Jahn-Teller and magnetic (high-spin to low-spin) effects in Fe and Cu cations, respectively. This explanation, however, does not seem plausible for the orbitally-inactive $ZnCr_2Se_4$ compound. On the contrary, the cubic-monoclinic transition in our case is most likely guided by steric effects, i.e. the favoring of denser structures with higher coordination numbers under pressure. As a result, the electronic and magnetic changes observed in the vicinity of the cubic-monoclinic transition from our DFT calculations (**Fig. 7**) appear to be consequences of the structural modification, rather than the driving force behind it.

Finally, we would like to address the apparent inconsistency in the transition pressures recorded in our Raman (**Fig. 2**) and IR studies of Rabia *et al.*[24] (insulator-metal transition in-between 11-14 GPa), and the cubic-monoclinic structural transition evidenced from our XRD investigation close to 17 GPa. It appears that the insulator-metal transition *precedes* the structural change, thus implying either (a) the pressure-induced metallization of the $Fd\bar{3}m$ phase prior to the structural transformation, or (b) the appearance of an intermediate metallic phase prior to the adoption of the high-pressure monoclinic structure. The first scenario is not supported by our DFT calculations, where the cubic phase remains insulating throughout the investigated pressure range [**Fig. 7(a)**]. As for the second possibility, our XRD study could not provide any evidence for the existence of a transient structure.

On the other hand, and considering that both Raman and IR methods "observe" the structure on a local scale whereas XRD serves as a more bulk probe[70], a plausible explanation behind the transition pressure discrepancies might be the following: the nucleation of the new high-pressure phase initiates on a local scale at about ~13 GPa, as determined by our Raman study. This high-pressure phase appears to be metallic, thus accoounting for the loss of the Raman signal. Further compression leads to the

development of the high-pressure phase at the expense of the starting $Fd\bar{3}m$; at 17 GPa, the volume of this high-pressure structure becomes sizeable enough to be detected in our XRD measurements. In other words, both Raman and XRD studies detect the same high-pressure phase, with the transition pressure difference rising from the diversity in the lattice range probed by these two methods. Such possibility would be also compatible with our DFT studies, where the cubic-monoclinic transition is accompanied by an insulator/metal transition (**Figs. 6, 7**).

IV. CONCLUSIONS

We have conducted high-pressure X-ray diffraction and Raman spectroscopic studies on the $ZnCr_2Se_4$ cubic spinel at room temperature. Our XRD study reveals one reversible structural transition near 17 GPa. This novel high-pressure phase could be best indexed with a structure resembling a AMo_2S_4-type phase, a distorted variant of the Cr_3S_4 structure. Our high-pressure Raman measurements revealed the substantial reduction of Raman signal above 12.5 GPa, thus hinting an insulator-metal transition. Our observation is consistent with a recent IR investigation[24]. Furthermore, our *ab initio* DFT study successfully reproduces this cubic-monoclinic structural transition. We computationally detected significant electronic and magnetic changes accompanying the structural modification, i.e. the substantial electronic band gap reduction (almost closure) and a halved Cr^{3+} magnetic moment.

ACKNOWLEDGEMENTS

We would like to thank Dr. S. Tkachev at GeoSoilEnviroCARS (Sector 13), APS-ANL for his assistance with the DAC gas loading. Portions of this work were performed at HPCAT (Sector 16), Advanced Photon Source (APS), Argonne National Laboratory. HPCAT operations are supported by DOE-NNSA under Award No. DE-NA0001974 and DOE-BES under Award No. DE-FG02-99ER45775, with partial instrumentation funding by NSF. The Advanced Photon Source is a U.S. Department of Energy (DOE) Office of Science User Facility operated for the DOE Office of Science by Argonne National Laboratory under Contract No. DE-AC02-06CH11357. Use of the COMPRES-GSECARS gas loading system was supported by COMPRES under NSF Cooperative Agreement EAR 11-57758 and by GSECARS through NSF grant EAR-1128799 and DOE grant DE-FG02-94ER14466. This research used resources of the Advanced Photon Source, a U.S. Department of Energy (DOE) Office of Science User Facility operated for the DOE Office of Science by Argonne National Laboratory under Contract No. DE-AC02-06CH11357.We would like to acknowledge support from NSF grant No. CMMI 1234777. We acknowledge use of computational resources from the Tandy Supercomputing Center and the Ohio Supercomputing Center[71]. This research has been partially supported by the Deutsche ForschungsgemeinschaftTransregional Collaborative Research Center Augsburg-

Munich (DFG TRR 80). Portion of this research was supported by the Michigan Space Grant Consortium, the Research Faculty Fellowship of Oakland University

*These authors contributed equally to this work: iliefthi@gfz-potsdam.de and Zhi.Liu@rockets.utoledo.edu.

†Current address: Helmholtz-Zentrum Potsdam, Deutsches GeoForschungsZentrum GFZ, Section 4.3, Telegrafenberg, 14473, Potsdam, Germany

‡Corresponding author: ywang235@oakland.edu

[1] M.D. Banus and M.C. Lavine, J. Sol. St. Chem. **1**, 109 (1969).

[2] C.N.R. Rao and K.P.R. Pisharody, Prog. Sol. St. Chem. **10**, 207 (1976).

[3] K.E. Sickafus, J.M. Wills, and N.W. Grimes, J. Am. Ceram. Soc. **82**, 3279 (1999).

[4] P.K. Baltzer, P.J. Wojtowicz, M. Robbins, and E. Lopatin, Phys. Rev. **151**, 367 (1966).

[5] T. Rudolf, C. Kant, F. Mayr, J. Hemberger, V. Tsurkan, and A. Loidl, New J. Phys. **9**, 76 (2007).

[6] R.J. Bouchard, Mater. Res. Bull. **2**, 459 (1967).

[7] Z. Wang, P. Lazor, S.K. Saxena, and G. Artioli, J. Sol. St. Chem. **165**, 165 (2002).

[8] Z. Wang, H.S.C.O. Neill, P. Lazor, and S.K. Saxena, J. Phys. Chem. Sol. **63**, 2057 (2002).

[9] D. Levy, V. Diella, A. Pavese, M. Dapiaggi, and A. Sani, Amer. Miner. **90**, 1157 (2005).

[10] A.M. Arevalo-Lopez, A.J. Dos Santos-Garcia, E. Castillo-Martinez, A. Duran, and M.A. Alario-Franco, Inorg. Chem. **49**, 2827 (2010).

[11] M. Chen, J. Shu, H.-K. Mao, X. Xie, and R.J. Hemley, Proc. Natl. Acad. Sci. U.S.A. **100**, 14651 (2003).

[12] A. Kyono and S. A. Gramsch and T. Yamanaka and D. Ikuta and M. Ahart and B. O. Mysen and H. K. Mao and R. J. Hemley, Phys. Chem. Miner. **39**, 131 (2012).

[13] W. Yong, S. Botis, S.R. Shieh, W. Shi, and A.C. Withers, Phys. Earth Planet. Inter. **196-197**, 75 (2012).

[14] I. Efthimiopoulos, Z.T.Y. Liu, S. V Khare, P. Sarin, T. Lochbiler, V. Tsurkan, A. Loidl, D. Popov, and Y. Wang, Phys. Rev. B **92**, 064108 (2015).

[15] R.E. Tressler, F.A. Hummel, and V.S. Stubican, J. Amer. Ceram. Soc. **56**, 648 (1968).

[16] R.E. Tressler and V.S. Stubican, J. Am. Ceram. Soc. **51**, 391 (1968).

[17] J. Hemberger, H.A.Krug von Nidda, V. Tsurkan, and A. Loidl, Phys. Rev. Lett. **98**, 147203 (2007).

[18] M. Hidaka, M. Yoshimura, N. Tokiwa, J. Akimitsu, Y.J. Park, J.H. Park, S.D. Ji,

and K.B. Lee, Phys. Stat. Sol. **236**, 570 (2003).

[19] T. Rudolf, C. Kant, F.Mayr, M.Schmidt, V.Tsurkan, J. Deisenhofer, and A. Loidl, Eur. Phys. J. B **68**, 153 (2009).

[20] T. Rudolf, C. Kant, F. Mayr, J. Hemberger, V. Tsurkan, and A. Loidl, Phys. Rev. B **75**, 052410 (2007).

[21] V. Felea, S. Yasin, A. Gunther, J. Deisenhofer, H.A.Krug von Nidda, S. Zherlitsyn, V. Tsurkan, P. Lemmens, J. Wosnitza, and A. Loidl, Phys. Rev. B **86**, 104420 (2012).

[22] X.L. Chen, Z.R. Yang, W. Tong, Z.H. Huang, L. Zhang, S.L. Zhang, W.H. Song, L. Pi, Y.P. Sun, M.L. Tian, and Y.H. Zhang, J. Appl. Phys. **115**, 83916 (2014).

[23] V.B. Sastry, N.A. Reddy, and K.S. Murthy, J. Phys. D Appl. Phys. **22**, 437 (1989).

[24] K. Rabia, L. Baldassarre, J. Deisenhofer, V. Tsurkan, and C.A. Kuntscher, Phys. Rev. B **89**, 125107 (2014).

[25] H.K. Mao, J. Xu, and P. Bell, J. Geophys. Res. **91**, 4673 (1986).

[26] A. Hammersley, S. Svensson, M. Hanfland, A. Fitch, and D. Hausermann, High Press. Res. **14**, 235 (1996).

[27] B.H. Toby, J. Appl. Crystallogr. **34**, 210 (2001).

[28] R.B. von Dreele and A.C. Larson, Los Alamos Natl. Lab. Rep. No. LAUR 86-748 (1994).

[29] F. Birch, Phys. Rev. **71**, 809 (1947).

[30] G. Kresse and J. Furthmuller, Comput. Mater. Sci. **6**, 15 (1996).

[31] G. Kresse and J. Furthmuller, Phys. Rev. B **54**, 11169 (1996).

[32] G. Kresse and J. Hafner, Phys. Rev. B **49**, 14251 (1994).

[33] G. Kresse and J. Hafner, Phys. Rev. B **47**, 558 (1993).

[34] P.E. Blochl, Phys. Rev. B **50**, 17953 (1994).

[35] G. Kresse and D. Joubert, Phys. Rev. B **59**, 1758 (1999).

[36] J.P. Perdew, J.A. Chevary, S.H. Vosko, K.A. Jackson, M.R. Pederson, D.J. Singh, and C. Fiolhais, Phys. Rev. B **48**, 4978 (1993).

[37] J.P. Perdew, J.A. Chevary, S.H. Vosko, K.A. Jackson, M.R. Pederson, D.J. Singh, and C. Fiolhais, Phys. Rev. B **46**, 6671 (1992).

[38] A. Zunger, S.H. Wei, L.G. Ferreira, and J.E. Bernard, Phys. Rev. Lett. **65**, 353 (1990).

[39] A. van de Walle, P. Tiwary, M. de Jong, D.L. Olmsted, M. Asta, A. Dick, D. Shin, Y. Wang, L.-Q. Chen, and Z.-K. Liu, Calphad-Computer Coupling Phase Diagrams Thermochem. **42**, 13 (2013).

[40] A. van de Walle, M. Asta, and G. Ceder, Calphad-Computer Coupling Phase Diagrams Thermochem. **26**, 539 (2002).

[41] A. van de Walle, Calphad-Computer Coupling Phase Diagrams Thermochem. **33**, 266 (2009).

[42] See Supplemental Material at [] for Raman-related data, the experimental and calculated structural data, construction parameters of the paramagnetic supercells, and a discussion of the bonding and charge tranfer properties for both the cubic and monoclinic phases of $ZnCr_2Se_4$.

[43] Z.T.Y. Liu, D. Gall, and S. V Khare, Phys. Rev. B **90**, 134102 (2014).

[44] Z.T.Y. Liu, X. Zhou, D. Gall, and S. V Khare, Comput. Mater. Sci. **84**, 365 (2014).

[45] Z.T.Y. Liu, X. Zhou, S. V Khare, and D. Gall, J. Phys. Cond. Mat. **26**, 25404 (2014).

[46] J.L. Roehl, Z.T.Y. Liu, and S. V Khare, Mater. Res. Express **1**, 25904 (2014).

[47] X. Zhou, J.L. Roehl, C. Lind, and S. V Khare, J. Phys. Cond. Mat. **25**, 75401 (2013).

[48] I. Efthimiopoulos, J. Kemichick, X. Zhou, S. V Khare, D. Ikuta, and Y. Wang, J. Phys. Chem. A **118**, 1713 (2014).

[49] S.P. Ong, W.D. Richards, A. Jain, G. Hautier, M. Kocher, S. Cholia, D. Gunter, V.L. Chevrier, K.A. Persson, and G. Ceder, Comput. Mater. Sci. **68**, 314 (2013).

[50] P.E. Blochl, O. Jepsen, and O.K. Andersen, Phys. Rev. B **49**, 16223 (1994).

[51] J. Zwinscher and H.D. Lutz, J. All. Comp. **219**, 103 (1995).

[52] D. Machon, P.F. McMillan, B. Xu, and J. Dong, Phys. Rev. B **73**, 094125 (2006).

[53] A.F. Goncharov and V. V Struzhkin, J. Raman Spectr. **34**, 532 (2003).

[54] D. Errandonea, R.S. Kumar, F.J. Manjon, V. V Ursaki, and I.M. Tiginyanu, J. Appl. Phys. **104**, 63524 (2008).

[55] Y. Amiel, G.K. Rozenberg, N. Nissim, A. Milner, M.P. Pasternak, M. Hanfland, and R.D. Taylor, Phys. Rev. B **84**, 224114 (2011).

[56] S. Hirai and W.L. Mao, Appl. Phys. Lett. **102**, 41912 (2013).

[57] I. Efthimiopoulos, A. Yaresko, V. Tsurkan, J. Deisenhofer, A. Loidl, C. Park, and Y. Wang, Appl. Phys. Lett. **104**, 11911 (2014).

[58] P. Vaqueiro, M.L. Kosidowski, and A. V Powell, Chem. Mater. **14**, 1201 (2002).

[59] P.J. Guillevic, J.-Y. Le Marouille, and D. Grandjean, Acta Cryst. **B 30**, 111 (1974).

[60] A. Waskowska, L. Gerward, J.S. Olsen, M. Marques, J. Contreras-Garcia, and J.M. Recio, High Press. Res. **29**, 72 (2009).

[61] N.M. Avram, M.G. Brik, and I. Sildos, Phys. Stat. Sol. **8**, 2585 (2011).

[62] A. Waskowska, L. Gerward, J.S. Olsen, M. Feliz, R. Llusar, L. Gracia, M. Marques, and J.M. Recio, J. Phys. Cond. Mat. **16**, 53 (2004).

[63] G. Busch, B. Magyar, and P. Wachter, Phys. Lett. **23**, 438 (1966).

[64] I. Efthimiopoulos, A. Yaresko, V. Tsurkan, J. Deisenhofer, A. Loidl, C. Park, and Y. Wang, Appl. Phys. Lett. **103**, 201908 (2013).

[65] A. Waskowska, L. Gerward, J.S. Olsen, A. Svane, G. Vaitheeswaran, and V. Kanchana, J. All. Comp. **578**, 202 (2013).

[66] P. Vaqueiro, A. V Powell, S. Hull, and D.A. Keen, Phys. Rev. B **63**, 064106 (2001).

[67] J. Wittlinger, S. Werner, and H. Schulz, Phys. Chem. Miner. **24**, 597 (1997).

[68] Y. Wang, I. Efthimiopoulos, T. Lochbiler, V. Tsurkan, J. Deisenhofer, and A. Loidl, in *APS March Meeting,* San Antonio (2015).

[69] A. Waskowska, L. Gerward, J. StaunOlsen, and and E. Malicka, J. Phys. Cond. Mat. **14**, 12423 (2002).

[70] J.M. Besson, J.P. Itie, A. Polian, G. Weill, J.L. Mansot, and J. Gonzalez, Phys. Rev. B **44**, 4214 (1991).

[71] Ohio Supercomputer Center: http://osc.edu/ark:/19495/f5s1ph73